Design and Simulation of a Microscale Magnetophoretic Device for the Separation of Nucleated Fetal Red Blood Cells from Maternal Blood.

Giuseppe Schiavone*[,1], Deirdre M. Kavanagh[2], Marc P.Y Desmulliez[2]

[1]Politecnico di Torino - Corso Duca degli Abruzzi, 24 - 10129 Torino, ITALY.
[2]MIcroSystems Engineering Centre, School of Engineering & Physical Sciences, Earl Mountbatten Building, Heriot-Watt University, Edinburgh EH14 4AS Scotland, UK

* Corresponding author: via Cervelli 15 70032 Bitonto (BA), ITALY;
Email: giuseppe_schiavone@hotmail.it

Abstract: Intense research has been carried out into methods that aim at harvesting fetal cells from maternal blood as substitutes to amniocentesis and chorionic villus sampling. Although much has been accomplished using well established techniques, a rapid and inexpensive method to separate fetal cells with great accuracy and efficiency to maximize cell yield is still required. This work focuses on the separation of fetal nucleated red blood cells from the maternal circulation based on their intrinsic magnetic properties. The design and simulation of a magnetophoretic separator is described, as it will be one of the stages of a lab-on-chip for non-invasive prenatal diagnosis (NIPD). Finite Element Analyses have been used to assist design choices and to confirm analytical results. A final layout has been validated for manufacturing and testing. Successful fabrication and positive test results of the device will constitute a further step towards the implementation of new techniques for NIPD.

Keywords: Magnetophoresis, MEMS, lab-on-chip, prenatal diagnosis.

1. Introduction

Prenatal diagnosis to determine pregnancy outcome is an important issue in public and medical communities. Intense research has been carried out into methods that aim at harvesting fetal cells from maternal blood as substitutes to amniocentesis and chorionic villus sampling. In that regard, a rapid and inexpensive method to separate fetal cells with great accuracy, sensitivity and efficiency to maximize cell yield is required. This work focuses on the separation of fetal nucleated red blood cells (NRBCs) in maternal circulation. Magnetophoretic separation is one of the separation methods researched in our group.

Magnetic separation of a pure cell population from a heterogeneous starting sample is a well established technique in biomedical research, mostly through the use of magnetic beads [1]. Recently, however, separation strategies have been investigated that do not require the use of expensive cell labels. One such method is magnetophoresis, which refers to the separation of cells based on their native magnetic properties. Magnetophoretic separators at the macroscale have had limited success as the generated fluxes are too small to have a significant effect on non-labelled biological cells. The design and simulation of a magnetic separator at the microscale is proposed for the separation of fetal NRBCs from maternal blood. While most cells are normally diamagnetic, deoxygenated adult and fetal red blood cells are paramagnetic when immersed in plasma, due to the positive contribution to the magnetic susceptibility gained with the reduction process [2]. Therefore, in the presence of a high magnetic field gradient, the magnetic forces, aided by a specifically designed microchannel architecture, will filter the blood sample.

2. Device

A microfluidic continuous flow device has been designed in a two stage continuous flow lab on chip system. Fetal NRBCs are separated from other cells in maternal blood through magnetic forces acting according to the different native magnetic properties of the bodies. NRBCs have the same magnetic properties as adult RBCs as they contain haemoglobin, they are one of the

earliest cellular stages in erythropoiesis and are nucleated. This provides a discrimination criterion as adult red blood cells are themselves anucleated. The first separation stage of the device should hence filter deoxygenated whole blood allowing fetal NRBCs and adult RBCs to flow together to the second stage, while discarding all other particles. The second filtration stage will be in charge of the separation of fetal nucleated cells from the adult anucleated ones, by means of capacitance measurements.

The proposed magnetophoretic separator is approximately 30mm long, and consists of a microfluidic channel with soft magnetic elements electrodeposited all along its length, on both sides. The device needs to be surrounded by structures providing a proper bias magnetic field which is then locally amplified into the microchannel by the soft magnetic elements. Figure 1 displays a schematic of the proposed device.

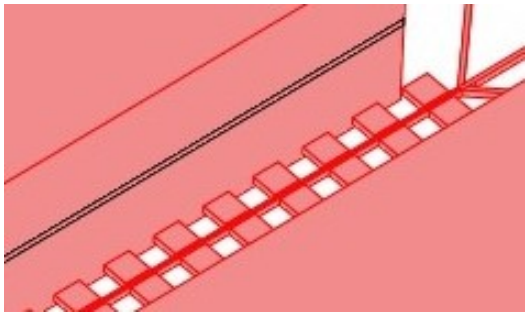

Figure 1. Microchannel with soft magnetic elements electrodeposited along the sides.

The external bias magnetic field is provided by permanent neodymium iron boron (NdFeB) magnets placed on either side of the device with magnetization oriented along the channel width direction. Permanent magnets are the preferred choice for the device as they make the magnetic structure completely passive and they do not suffer from heating. The channel is 50µm wide, about 20mm long and 50µm thick, with one inlet to inject deoxygenated whole blood and three outlets, two lateral ones for fetal NRBCs and adult RBCs collection and a central outlet for white blood cells (WBCs) collection. Square cross sectioned 300µm by 300µm by 50µm NiFe alloy elements are embedded with a spacing of 300µm from each other and of 10µm from the channel. The external flux provided by the permanent magnets magnetises the NiFe (Permalloy) elements, creating a field pattern varying in space, which gives rise to a magnetic force on the cells flowing through the microchannel. Therefore the magnetic forces in combination with microchannel architecture will filter the blood sample.

The channel is divided into two halves all along its length by a patterned splitting structure which prevents cells from occupying the middle part, which, for symmetry reasons, is characterized by a minimum of the magnetic field and hence where only very small magnetic forces can be observed. This is illustrated in figure 2.

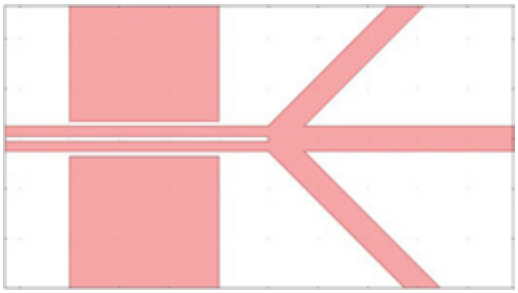

Figure 2. Splitting structure inside the microchannel.

The splitting structure is 10µm wide, so that each of the halves of the channel is 20µm wide. This both allows cells to flow one at a time through the device, minimizing their interactions with each other, and also adds a converging component to the fluid velocity in correspondence of the edge of the structure, favoring successful separation.

The device is fabricated by photolithography employing the negative photoresist SU8 50 to pattern the structures, plus electroplating for the Permalloy elements. Sealing is achieved by covering the whole device with another wafer with SU8 spun on it.

3. Theory

3.1 Magnetic force

The magnetic susceptibility χ_c of red blood cells depends on the oxidation state of the haemoglobin molecules. RBCs in a normal state exhibit an extremely weak diamagnetic behaviour as χ_c is negative and quite close to

zero. As experimentally measured, the reduction process confers a paramagnetic component to χ_c, resulting in a higher value, even if still negative [2]. Both plasma and white blood cells have diamagnetic behaviour too.

Cells can be modelled as a collection of magnetic dipoles which eventually collapse into an effective magnetic dipole, and on which forces rising from high magnetic field gradients can act. Given a region characterised by a magnetic field, the magnetic force on a magnetised body can be expressed as

$$\overrightarrow{F_m} = \int_V \left(\overrightarrow{M} \cdot \vec{\nabla}\right)\vec{B}_{ext}\, \mathrm{d}\vec{v}, \qquad (1)$$

where V is the volume of the body, M its magnetization, and B_{ext} the magnitude of the external magnetic flux density [3]. Experimental results show that saturation does not occur in blood cells for any value of the applied magnetic field in any reasonable range. M can therefore be modeled with a linear magnetization response curve with respect to the field inside the cell H_{in}, the slope given by the experimentally found χ_c. Being χ_c quite low for any kind of cell (in the order of magnitude of $10^{-6} \div 10^{-5}$), the demagnetization field for cells can be neglected, resulting in a linear magnetization characteristic with respect to the external applied magnetic field:

$$\begin{aligned} &\overrightarrow{M} = \chi_c \overrightarrow{H}_{in} = \chi_c \left(\overrightarrow{H}_{ext} + \overrightarrow{H}_{d,c}\right) = \\ &= \chi_c \left(\overrightarrow{H}_{ext} - N_{d,c}\overrightarrow{M}\right) \qquad , \qquad (2) \\ &\overrightarrow{M} = \frac{\chi_c}{\chi_c N_{d,c} + 1}\overrightarrow{H}_{ext} \approx \chi_c \overrightarrow{H}_{ext} \end{aligned}$$

where $H_{d,c}$ and $N_{d,c}$ are respectively the demagnetization field and the demagnetization factor relative to the cell.

The effect of the medium the cells are flowing through can then be considered by substituting the native magnetic susceptibility of cells χ_c with the factor $(\chi_c - \chi_f)$ in (2), corresponding to the magnetic susceptibility difference between the body and the medium [4].

The magnetically active structures in the device will be sized as to have dimensions greater enough than those of cells, so that the variations of the magnetic field will not be considerable within the volume of a single cell. This leads to drop the integration in (1) and replace it with a multiplication factor V_c corresponding to the volume of the modelled cell.

By applying all these considerations and expressing the external applied magnetic flux density using the corresponding magnetic field value through the magnetic permeability of the medium μ_f and a final expression for the magnetic force can be derived from (1):

$$\overrightarrow{F_m} = \mu_f \left(\chi_c - \chi_f\right) V_c \left(\overrightarrow{H}_{ext} \cdot \vec{\nabla}\right)\overrightarrow{H}_{ext}. \qquad (3)$$

Susceptibility values reported in [6] confirm this formula, numerically $\chi_{deoxi,rbc} = -3.9 \cdot 10^{-6}$, $\chi_{wbc} = -9.2 \cdot 10^{-6}$ and finally $\chi_f = -7.7 \cdot 10^{-6}$. Therefore arising forces of opposite sign result in different cells accelerating in opposite directions. Furthermore, the expression depends both on the external magnetic field and its gradient, hence making it an ideal condition to have the microchannel of the device characterized by a strong and reliably uniform bias field plus spatial variations to have the gradient contribute to the magnitude of the force.

3.2 Magnetic field pattern

A proper bias field source must wrap the device in order to correctly determine the strong field direction, which must be transversal with respect to the channel length (y axis throughout the notation). Two permanent magnets rectangular in shape are employed as the source of the bias field, as shown in figure 3.

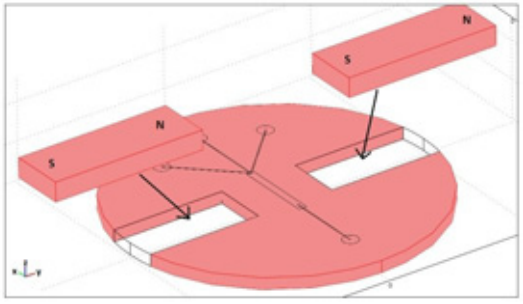

Figure 3. Scheme showing placement of the permanent magnets.

The magnets act on the soft magnetic elements by magnetising them along the *y* axis direction. The magnetic properties of NiFe elements have been measured experimentally and used for modelling. The reaction to the external field gives rise to locally confined strong amplifications which modify the magnetic field pattern in the microchannel. The NiFe elements are modelled through a linear magnetisation response curve with respect to the internal field H_{in} with sudden saturation to the maximum value $M_s = 5.97 \cdot 10^5$ A·m^{-1} given by experimental data. Recalling (2), and acknowledging that the magnetic susceptibility of the electrodeposits χ_m is very high, below saturation the response can be written as

$$\begin{aligned} \vec{M} &= \chi_m \vec{H}_{in} = \chi_m \left(\vec{H}_{ext} + \vec{H}_d \right) = \\ &= \chi_m \left(\vec{H}_{ext} - N_d \vec{M} \right) \\ \vec{M} &= \frac{\chi_m}{\chi_m N_d + 1} \vec{H}_{ext} \approx \frac{\vec{H}_{ext}}{N_d} \end{aligned} \quad , \qquad (4)$$

where $H_{d,c}$ and $N_{d,c}$ are respectively the demagnetization field and the demagnetization factor relative to the electrodeposits. Tables in [5] report $N_d \approx 0.2$ for the *x* (parallel to the channel length) and *y* (parallel to the channel width) axes, and $N_d \approx 0.7$ for the *z* axis (parallel to the channel thickness). If the external field is high enough, the elements saturate to the maximum value M_s. The complete response can thus be summarized as follows:

$$\vec{M} = \begin{cases} \dfrac{\vec{H}_{ext}}{N_d} & \text{if } H_{ext} \le N_d M_s \\ \vec{M}_s & \text{if } H_{ext} > N_d M_s \end{cases} . \qquad (5)$$

3.3 Fluidic drag force

In low Reynolds number and Stokes flow regime, pressure driven fluid flow will have a parabolic shaped velocity profile, with null *y* and *z* components. Under the assumption of spherical shaped cells the drag force exerted by the fluid flowing with a velocity $v_f(y,z)$ can be written as:

$$\vec{F}_f = -6\pi\eta R_c \left(\vec{v}_c - \vec{v}_f \right), \qquad (6)$$

where η is the dynamic viscosity of the fluid, R_c is the radius of the cell and v_c its velocity.

3.4 Equation of motion

The performance of device can be assessed by tracing the trajectories of cells injected into the microchannel, when those are subjected to the modelled forces. RBCs (and NRBCs) starting from any position in the cross section of the microchannel must end their path in one of the side outlets while WBCs starting from any position in the cross section of the microchannel must end their path in the central outlet. This is verified by solving the equation of motion

$$\vec{F}_f + \vec{F}_m = m_c \frac{\partial \vec{v}_c}{\partial t} , \qquad (7)$$

where m_c is the mass of a cell, and plotting the trajectory $r(t)$ for a series of initial conditions $v_{cx,0}$, $v_{cy,0}$ and $v_{cz,0}$ for the velocities, and $r_{cx,0}$, $r_{cy,0}$ and $r_{cz,0}$ for the positions. A RBC is considered separated when it reaches the channel wall, it will then roll along the wall until reaching the edge of the main channel and eventually the proper outlet. Let the distance along the *x* axis a cell needs to travel to achieve separation, i.e. to reach its proper outlet, be called separation length. Yielding deoxygenated RBCs and WBCs similar values of the factor $(\chi_c - \chi_f)$, and being the latter bigger than the former, the worst case scenario will depict a RBC having to travel the whole distance along the *y* axis from the splitting structure to the channel wall, under the action of the magnetic force. In the meanwhile the fluidic force will keep on pushing it forward along the *x* axis, increasing the separation length. Thus for a given fluid velocity, the separation length corresponding to this case will determine the overall length of the device, so that it will guarantee separation for any cell starting the separation path from any position.

4. Use of COMSOL Multiphysics

Simulations were carried out to assist design choices. Finite Element Method analyses implemented using the Magnetostatics and the Incompressible Navier-Stokes application modes of COMSOL Multiphysics have been used to

validate analytical results. The simulation strategy accounts for the following steps:

1. demonstration of the magnetic excitation of NiFe elements by the permanent magnets to correctly size the structures;
2. simulation of the fluid velocity profile in the microchannels;
3. multiphysics simulation with both modules to retrieve the magnetic field pattern and the fluid velocity profile in the microchannel;
4. use this data to perform a particle tracing postprocessing plot in order to monitor the functionality of the device and size its length.

For the magnetostatics simulations the no currents module was loaded. Permanent magnets are modelled as bodies with magnetization uniformly directed along the y axis and magnetic permeability was provided in manufacturer's datasheets. The NiFe soft magnetic elements are modelled by imposing the magnetization response (5) as arbitrary $M(H)$ relation in the subdomain settings. An environment is drawn encapsulating the whole device to allow the magnetic field to have a proper distribution in the surrounding space. Next a symmetry boundary was set on the xz plane corresponding to $y = 0$, along the midline of the microchannel. The boundary conditions on the interior boundaries are already set by default to continuity, while magnetic insulation was set on the external boundaries of the environment except for the symmetry one, where the zero potential condition was set. This properly models the device conditions, since the $y = 0$ plane is characterised by either magnetic field minima or maxima for symmetry reasons, while the other external boundaries are drawn far enough from the field sources to have a null magnetic field normal component. The computational power saved thanks to symmetry conditions was redeployed to using a more refined meshing to achieve smoother plots.

As for the fluidic simulations, the incompressible Navier-Stokes module was loaded. The microchannel is the only subdomain active in this module, values obtained from literature are set as subdomain settings for the density and viscosity of plasma [6]. The same symmetry boundary is exploited as for the magnetic simulations. The no-slip condition is set on all the walls of the channel, except for the inlet, where various values for the normal fluid velocity were set, and for the outlets, where zero pressure was imposed.

The derived expression (3) for the magnetic force on cells was set as a subdomain expression of the microchannel subdomain in the proper expression field of Comsol. In this way the magnetic force expression can be plotted as a vector field representing the magnetic force acting on a cell as a function of its position in the microchannel volume. This is possible as expression (3) does not depend on the velocity of the cells as does expression (7) for the drag force.

Once the whole problem is solved, numerical data for the magnetic force and the fluid velocity profile are available and stored in memory. Hence a particle tracing postprocessing plot can be executed by selecting parameters again as from [6] for the cells, and by assigning the derived expressions (3) and (7) as the force expressions for the solver. A series of initial conditions can be imposed for the positions of the simulated RBCs, spanning the whole width of the channel in order to seek the dependency of the separation length on the starting distance from the channel wall.

5. Results

Various separating distances and placements were investigated in order to achieve the best magnetic field pattern.

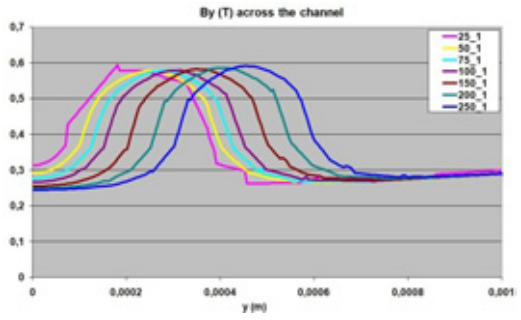

Figure 4. Graph showing various displacements of the NiFe elements.

Figure 4 shows the effect of displacing the NiFe elements with respect to the microchannel on the magnetic field pattern. The y component of the

flux density B_y was plotted along the y axis, as to cross transversally one of the elements and the microchannel. The origin of the y axis is the middle of the channel, where a magnetic field minimum clearly stands. The optimal gap distance of 10μm was eventually chosen to reinforce the magnitude of the field penetrating the microchannel.

For such a distance, figure 5 shows a plot of the same quantity B_y along the x axis, at a fixed y position close to the channel wall.

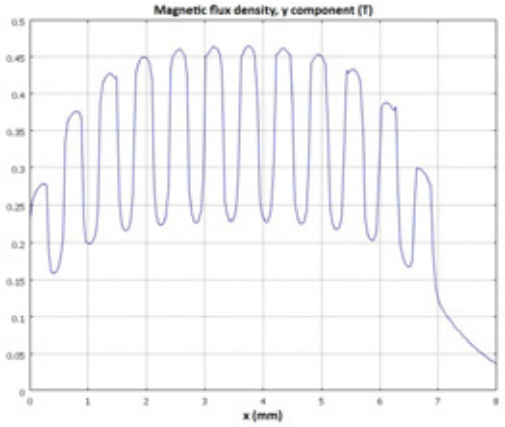

Figure 5. Graph depicting B_y along the channel length. This field is the superimposition of the bias field from the magnets plus the local amplifications due to the magnetization of the NiFe elements.

It is clear from figure 5 how both the magnetic field magnitude and its variations contribute to the magnetic force as from expression (3). The complexity of expression (3) does not allow to intuitively understand the behaviour of the cells in the device, as there are too many directional dependencies, and each of the three force components depends on all the three field components.

Plots of the magnetic forces are also provided, allowing a better understanding of the functionality of the device. Figure 6 shows a plot of the transversal component of the magnetic force $F_{m,y}$ (the one in charge of the separation) along the x axis, parallel to the channel length, for a fixed y value close to the channel wall.

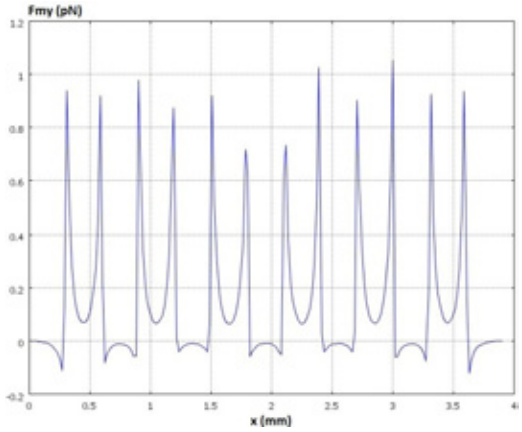

Figure 6. $F_{m,y}$ along the channel length. The net force underpins the feasibility of separation. Forces are positive on average on the positive y region, thus red blood cells are pushed towards the channel wall as expected.

Figure 7 shows a plot of the same component of the force along the y axis, for an x value corresponding to the centre of a NiFe element (the whole channel width was simulated, without exploiting symmetry). The splitting structure prevents cells from occupying the middle of the channel, so field values in the middle part of the plot never play a role.

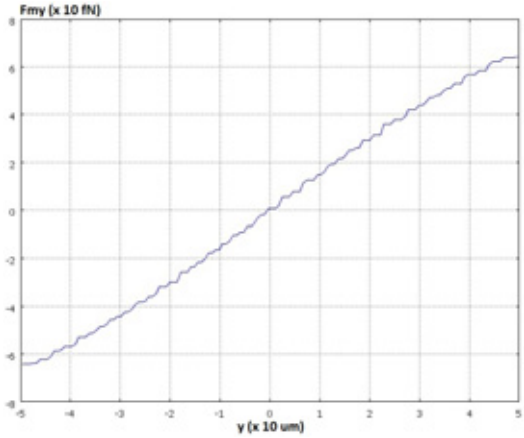

Figure 7. $F_{m,y}$ along the channel width. The sign of the force switches crossing the middle of the channel, determining an instable equilibrium point which allows separation, since red blood cells on the left will be pushed further left, and viceversa.

As for the fluid velocity profile, figure 8 shows results as expected from modelling.

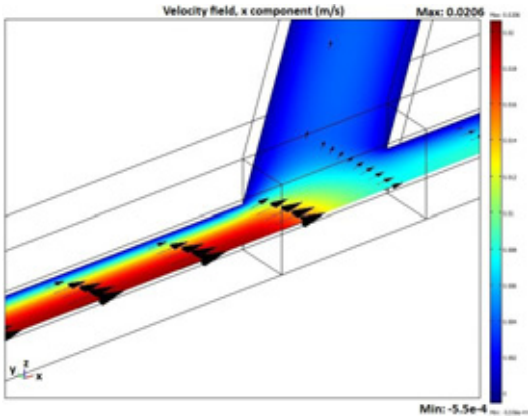

Figure 8. Slice plot of the fluid velocity in the half portion of the microchannel. The profile is parabolic as expected.

The final step in the design is to determine the separation length required based on the starting position of a cell, in order to size the length of the channel. This task is accomplished through particle tracing, which allows the trajectories of simulated cells through the microchannel to be plotted. By varying the initial conditions of simulated cells for the particle tracing, it is possible to plot the separation length as a function of the starting width of a cell. This can be done for various imposed fluid velocities at the inlet, yielding different results as shown in figure 10.

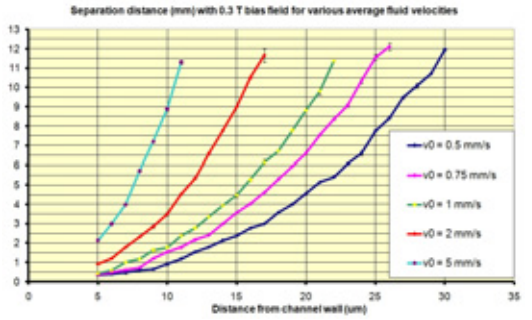

Figure 10. Separation length as a function of the starting width of cells, for various normal fluid velocities at the inlet.

For a given fluid velocity a different device length has to be considered, as a slower moving fluid allows for a shorter separation length. The resulting plots are then used to decide the overall device length which guarantees separation for any cell entering the device, according to the particular inlet fluid velocity.

7. Conclusions

This paper presents results obtained by Finite Element Analyses of a microscale magnetophoretic separator for blood cell separation. A final layout has been validated for manufacturing and testing. Successful fabrication and positive test results of the device will constitute a further step towards the implementation of new techniques for NIPD.

8. References

1. JY. Wang, Fetal nucleated erythrocyte recovery: Fluorescent activated cell sorting based positive selection using anti-gamma globin versus magnetic activated cell sorting using anti-cd45 depletion and anti-gamma globin positive selection, *Cytometry*, **39**, 224 – 230 (2000)
2. L. Sakhnini and R. Khuzaie, Magnetic behavior of human erythrocytes at different hemoglobin states, *Eur Biophys J*, **30**,(2001)
3. E. P. Furlani, *Permanent magnet and electromechanical devices – materials, analysis and applications*. Academic Press (2001)
4. T. P. Jones, *Electromechanics of Particles*. Cambridge University Press, Cambridge, UK, (1995)
5. Chen Du-Xing, Enric Pardo, and Alvaro Sanchez, Demagnetizing factors of rectangular prisms and ellipsoids. *IEEE TRANSACTIONS ON MAGNETICS*, **38**, (2002)
6. E. P. Furlani, Analysis of particle transport in a magnetophoretic microsystem. *Journal of Applied Physics*, **99**, (2006)